Acidic “Water-in-Salt” Electrolyte Enables a High-Energy Symmetric Supercapacitor Based on Titanium Carbide MXene

Yuan, Chengzhi; Chen, Chaofan; Yang, Zhiwei; Cheng, Jiaji; Weng, Ji; Tan, Shuhui; Hou, Renzhong; Cao, Tao; Tang, Zeguo; Chen, Wei

DOI
10.1021/acsami.4c08094

Publication date
2024

Document Version
Final published version

Published in
ACS Applied Materials and Interfaces

ACS APPLIED MATERIALS & INTERFACES

www.acsami.org Research Article

Acidic "Water-in-Salt" Electrolyte Enables a High-Energy Symmetric Supercapacitor Based on Titanium Carbide MXene

Chengzhi Yuan,[#] Chaofan Chen,[#] Zhiwei Yang,[#] Jiaji Cheng,* Ji Weng, Shuhui Tan, Renzhong Hou, Tao Cao, Zeguo Tang, Wei Chen, Baomin Xu,* Xuehang Wang,* and Jun Tang*

Cite This: *ACS Appl. Mater. Interfaces* 2024, 16, 55189−55197 Read Online

ACCESS | Metrics & More | Article Recommendations | Supporting Information

ABSTRACT: Titanium carbide MXene, $Ti_3C_2T_x$, exhibits ultrahigh capacitance in acidic electrolytes at negative potentials yet poor stability at positive potentials, resulting in low-energy densities for $Ti_3C_2T_x$-based symmetric supercapacitors. Utilizing "water-in-salt" electrolytes has successfully expanded the stable operation potential window of MXenes. However, this advancement comes at the cost of sacrificing their high capacitance in acidic electrolytes. In this work, we report an acidic "water-in-salt" (AWIS) electrolyte composed of sulfuric acid and saturated lithium halide, which effectively doubled the energy density of the $Ti_3C_2T_x$-based symmetric supercapacitor compared to those with bare acidic electrolytes. Specifically, the AWIS electrolyte successfully expanded the voltage window of the symmetric device to 1.1 V. A high specific capacitance of 112.34 F g^{-1} (at 10 mV s^{-1}) was obtained due to the presence of proton redox. As a result, the symmetric device achieved a high-energy density of 19.1 Wh kg^{-1} and a high capacitance retention of 96.3% after 10,000 cycles. This work demonstrates the importance of designing stable and redox-active electrolytes for high-energy MXene-based symmetric supercapacitors.

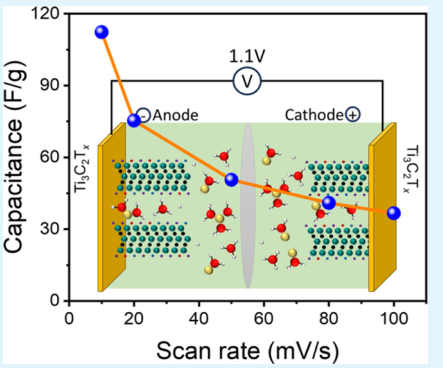

KEYWORDS: *titanium carbide MXene, acidic water-in-salt electrolyte, symmetric supercapacitors, proton redox*

INTRODUCTION

Two-dimensional (2D) transition-metal carbides and/or nitrides, known as MXenes, are promising electrode materials for supercapacitors due to their high specific capacitance and outstanding rate capability.[1−8] $Ti_3C_2T_x$, the most studied MXene, has shown remarkably high volumetric capacitance exceeding 1500 F cm^{-3}, which is among the highest values of the reported electrode materials for supercapacitors. It can also deliver a high rate capability in which capacitance retention exceeding 91.7% was reported with the macroporous $Ti_3C_2T_x$ electrode at a scan rate of 1000 mV s^{-1}.[1] In addition, MXene has many applications in the field of batteries.[9−13] However, the high performance of $Ti_3C_2T_x$ in acidic electrolytes is only applicable in the negative potential range (vs open-circuit potential).[14,15] Anodic oxidation of $Ti_3C_2T_x$ takes place when the potential exceeds a certain positive threshold, limiting the application of $Ti_3C_2T_x$ as a positive electrode.[16] As the formula $E = 1/2CV^2$ indicates, both the capacitance and voltage window are crucial for achieving high-energy-density devices.[17] The weak oxidation resistance of $Ti_3C_2T_x$ MXenes in acidic electrolytes greatly restricts their operational voltage windows when used as electrodes of symmetric supercapacitors, leading to moderate energy densities.

To broaden the operation voltage window for $Ti_3C_2T_x$-based supercapacitors, possible solutions lie in assembling asymmetric devices by pairing $Ti_3C_2T_x$ negative electrodes with other positive electrodes and/or optimizing electrolytes to stabilize MXene electrodes at positive potentials.[18−20] Jiang et al. developed a $Ti_3C_2T_x$−RuO_2 asymmetric capacitor, which offered a voltage window of 1.5 V and an energy density of 37 μWh cm^{-2} with a power density of 40 mW cm^{-2}.[21] MnO_2 was also paired with $Ti_3C_2T_x$ to make an asymmetric device that expanded the voltage window to 1.5 V.[22] The energy and power densities of the asymmetric device reached 6.4 Wh kg^{-1} and 1107.7 W kg^{-1}, respectively. MXene has been combined with a double-layer capacitive carbon material and other pseudocapacitive materials. When paired with rGO, the energy and power density of $Ti_3C_2T_x$−rGO asymmetric devices reached 8.6 mWh cm^{-3} and 0.2 W cm^{-3}, respectively.[23] However, the total capacitance and the rate performance of an asymmetric supercapacitor are limited by the electrode with a lower specific capacitance and worse rate capability, respectively.[24] Additionally, using different electrode materials may lead to uneven expansion and contraction during charging and discharging, resulting in performance degradation and

Received: May 16, 2024
Revised: September 23, 2024
Accepted: September 24, 2024
Published: October 7, 2024

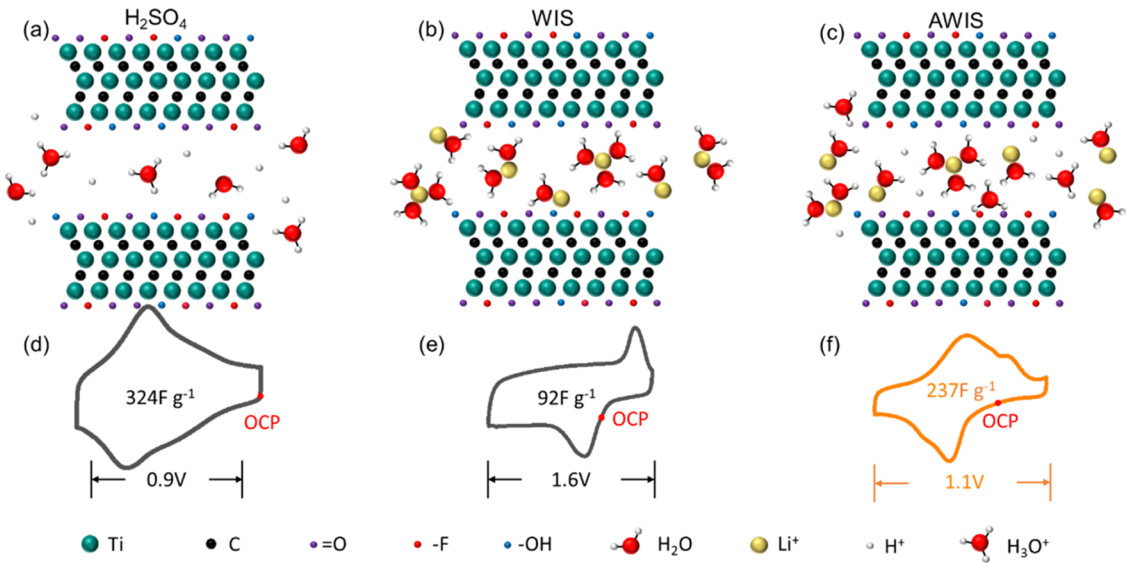

Figure 1. (a–c) Charge storage mechanism illustrations and (d–f) the corresponding cyclic voltammetry curves of $Ti_3C_2T_x$ in H_2SO_4, WIS and AWIS electrolytes, respectively.

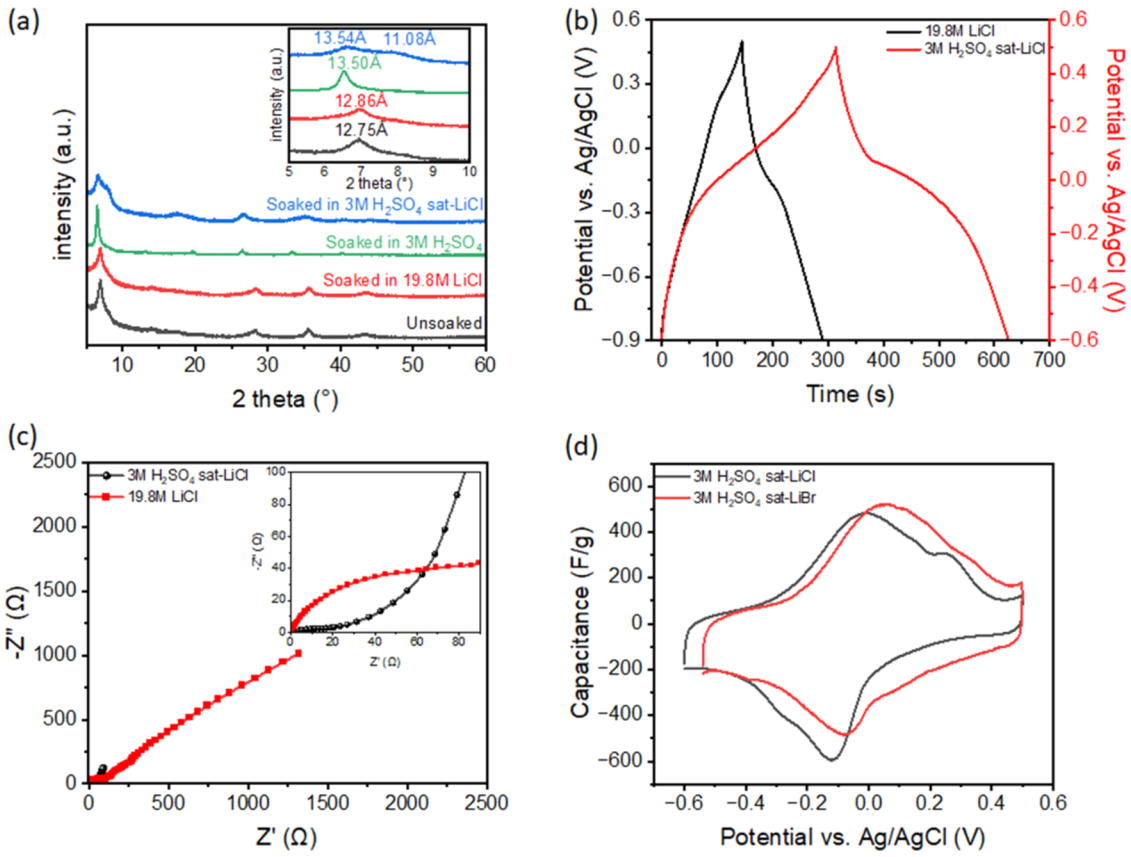

Figure 2. (a) XRD patterns of vacuum-evacuated $Ti_3C_2T_x$ after 12 h of soaking in 19.8 M LiCl, 3 M H_2SO_4, and 3 M H_2SO_4 sat-LiCl; (b) galvanostatic charge–discharge curves of 19.8 M LiCl and 3 M H_2SO_4 sat-LiCl; (c) Nyquist plot of sat-LiCl and 3 M H_2SO_4 sat-LiCl; (d) cyclic voltammograms of $Ti_3C_2T_x$ collected in 3 M H_2SO_4 sat-LiCl and 3 M H_2SO_4 sat-LiBr.

shortened lifespan.[25−27] In contrast, symmetric supercapacitors exhibit good stability, cycling consistency, and ease of manufacturing.[28,29] Using "water-in-salt" (WIS) electrolytes has been reported to enhance the electrochemical oxidation stability of MXene up to 0.8 V vs Ag, which can expand the voltage window of MXene-based symmetric cells. A large voltage of 1.6 V was achieved in MXene-based symmetric supercapacitors when a saturated LiCl aqueous solution was used as the electrolyte. However, the capacitance of the device is moderate, measuring at only 26 F g^{-1}, due to the weak surface redox activity with Li-ions in the WIS electrolyte.[30] It would be more ideal to have an electrolyte that can expand the potential window while remaining redox-active when paired with an MXene electrode.

https://doi.org/10.1021/acsami.4c08094
ACS Appl. Mater. Interfaces 2024, 16, 55189−55197

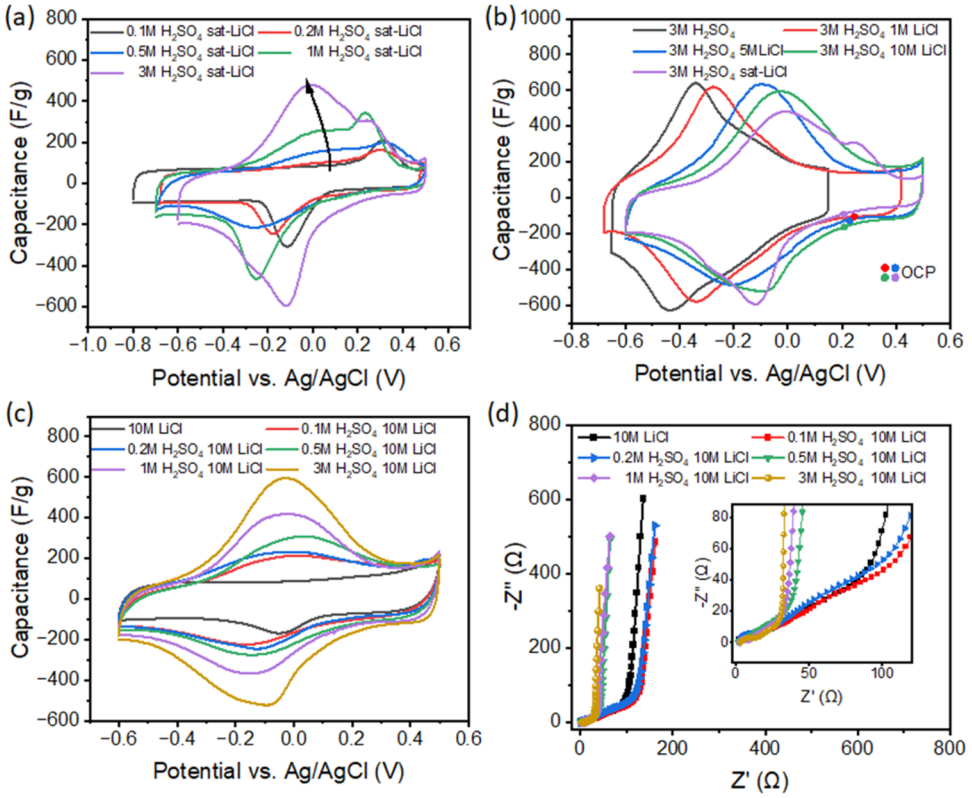

Figure 3. (a) Cyclic voltammograms of $Ti_3C_2T_x$ after vacuum filtration in different concentrations of H_2SO_4 with saturated LiCl at 2 mV s^{-1}; (b) cyclic voltammograms of $Ti_3C_2T_x$ in 3 M H_2SO_4 with different concentrations of LiCl at 2 mV s^{-1}; (c) cyclic voltammograms and (d) Nyquist plots of $Ti_3C_2T_x$ in 10 M LiCl with different concentrations of H_2SO_4 at 2 mV s^{-1}.

Herein, an acidic "water-in-salt" (AWIS) electrolyte is developed for broadening the potential window of $Ti_3C_2T_x$ while retaining its high capacitance. Due to the presence of protons, strong proton surface redox can occur on MXene, leading to a high capacitance of 276.84 F g^{-1} at 2 mV s^{-1}. As a result, high-energy density is achieved in $Ti_3C_2T_x$-based symmetric supercapacitors, which also deliver high rate capability and long cycling life. The development of acidic WIS electrolytes offers a new avenue for the advancement of MXene-based high-energy symmetric devices.

RESULTS AND DISCUSSION

The electrochemical performance of $Ti_3C_2T_x$ is predominantly influenced by the electrolyte, which ultimately determines its charge storage mechanism.[31] $Ti_3C_2T_x$ exhibits pseudocapacitive properties with broad and less-separated redox peaks in acidic electrolytes (Figure 1a), which can be attributed to the conversion between ═O and −OH functional groups upon proton (de)intercalation, resulting in a high capacitance of 324 F g^{-1}.[32] Nevertheless, the potential window of $Ti_3C_2T_x$ is constrained to 0.9 V in H_2SO_4, with a significant portion of its range being more negative compared to its open-circuit potential (OCP). In dilute neutral aqueous electrolyte, MXenes deliver moderate capacitance due to the absence of redox reactions.[33] By increasing the concentration of neutral aqueous electrolyte, an extra desolvation-free intercalation process is initiated when $Ti_3C_2T_x$ is charged in 19.8 M LiCl WIS electrolytes.[30] Moreover, a wide operating potential window of 1.6 V can be achieved in the WIS electrolyte, which is ascribed to the reduction of free water molecules. However, the capacitance is still low (92 F g^{-1}) in WIS electrolyte, since no Faradaic reaction occurred when protons are absent (Figure 1b).[30,34] The cyclic voltammetry (CV) curves of MXene in 19.8 M LiCl WIS electrolyte exhibit a pair of distinctive redox peaks with large peak separations of 0.53 V (ΔE_p) (Figure 1d,e), corresponding to the (de)intercalation of solvated Li^+.[30] By mixing H_2SO_4 with concentrated LiCl, we formulated a novel AWIS electrolyte. $Ti_3C_2T_x$ shows two oxidation peaks in AWIS, possibly attributed to the characteristic peaks of H^+ and Li^+ intercalation (Figure 1f). Taking advantage of the strong proton surface redox enabled by an acidic environment and enhanced oxidation stability facilitated by WIS, $Ti_3C_2T_x$ delivers a high capacitance of 237 F g^{-1} within a broad potential window of 1.1 V in AWIS.

$Ti_3C_2T_x$ films show a restacking layered structure, as shown in Figure S1. In order to verify the feasibility of mixing H_2SO_4 and LiCl WIS electrolytes, $Ti_3C_2T_x$ was immersed in each of the three electrolytes for 12 h. The X-ray diffraction (XRD) image (Figure 2a) shows that the interlayer spacing of $Ti_3C_2T_x$ remains essentially unchanged after immersion in the WIS electrolyte. The *d*-spacing increased to 13.50 Å after immersion in H_2SO_4, which is attributed to the insertion of a large amount of H_3O^+.[35] After immersion in the AWIS electrolyte, two (002) peaks appeared, which may be attributed to the insertion of two cations.

The electrochemical performance of $Ti_3C_2T_x$ in AWIS electrolytes was investigated by using a three-electrode setup. The galvanostatic charge−discharge (GCD) test (Figure 2b) shows that AWIS possesses a much better charge/discharge duration and at the same time has a similar and distinct plateau, which corresponds to the redox peaks shown in the CV curves. Based on the Nyquist plots in Figure 2c, the

https://doi.org/10.1021/acsami.4c08094
ACS Appl. Mater. Interfaces 2024, 16, 55189−55197

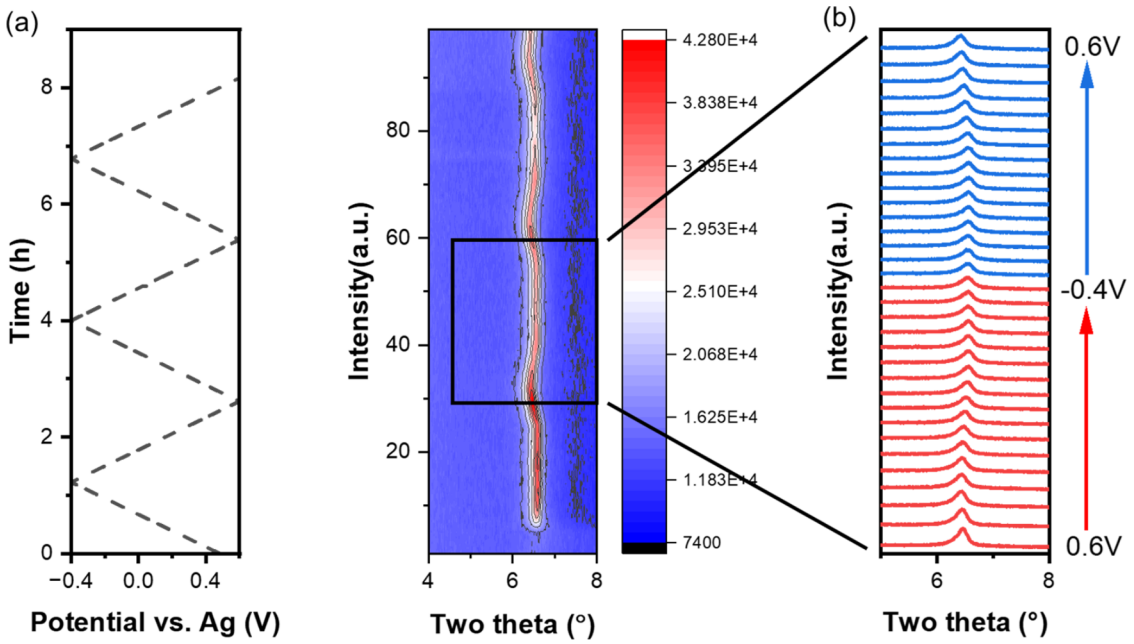

Figure 4. *In situ* XRD test images of $Ti_3C_2T_x$ in 3 M H_2SO_4 and 10 M LiCl. (a) *In situ* XRD image during electrochemical cycling; (b) *in situ* XRD image of the second cycle.

semicircular curves of the class in the high-frequency region are substantially smaller after the addition of H^+, implying lower charge-transfer resistance in AWIS. In the low-frequency region, the slope of AWIS is larger compared to that of 19.8 M LiCl, which also reflects a more ideal capacitive electrochemical process or a surface-reaction-controlled Faradaic process.[36]

To validate the universality of the high performance of $Ti_3C_2T_x$ in AWIS, 3 M H_2SO_4 was further mixed with a saturated LiBr electrolyte (sat-LiBr). As shown in Figure 2d, a potential window of 1.0 V and a capacitance of 260.7 F g^{-1} are achieved. It is worth noting that even the absolute value of the potential window is close for $Ti_3C_2T_x$ in H_2SO_4 and AWIS, but the OCPs are quite different. The maximum applicable potential of $Ti_3C_2T_x$ in AWIS electrolyte is approximately 0.3 V above the OCP, in a potential range of −0.6 to 0.5 V (vs Ag/AgCl in saturated KCl) (an Ag/AgCl reference electrode was used throughout this study unless specifically stated). The potential window is increased by 20% compared to 3 M H_2SO_4, and the capacitance is increased by 121.25% compared to that of WIS electrolyte. Additionally, the electrochemical charging/discharging process of $Ti_3C_2T_x$ is highly reversible in 3 M H_2SO_4 and sat-LiCl and in 3 M H_2SO_4 and sat-LiBr, with Coulombic efficiencies of 99.08 and 99.25%, respectively (Figure S2a,b). Moreover, ΔE_p between the oxidation and reduction peaks in AWIS is only 0.11 V, suggesting better kinetics.[37]

To reveal the impact of electrolyte compositions on the electrochemical properties of $Ti_3C_2T_x$, we first compared the CV curves for $Ti_3C_2T_x$ in H_2SO_4 and sat-LiCl AWIS with varying H_2SO_4 concentrations. As shown in Figure 3a, the peak intensity of $Ti_3C_2T_x$ around 0 V gradually increases as the H_2SO_4 concentration increases, indicating an enhanced redox reaction, and reaches the maximum when 3 M H_2SO_4 is applied. Meanwhile, the peak separation changes with H^+ concentration, which indicates that the introduction of H^+ may affect the Li^+ intercalation process. Nevertheless, the potential window becomes narrower with an increased H_2SO_4 concentration, especially within the negative potential region. In addition, chronoamperometry data and Nyquist plots (Figure S3) show that for the 3 M H_2SO_4 and sat-LiCl electrolyte under Li^+ saturation, steady-state leakage currents were tested at different potentials, and the steady-state leakage currents were found to be relatively large at 0.2 and 0.5 V (0.1 A g^{-1}), and the Nyquist plot also showed abnormality at −0.6 V.

The influence of Li^+ ion insertion on the electrochemical performance of $Ti_3C_2T_x$ was further evaluated by adding different concentrations of LiCl to 3 M H_2SO_4. The potential window keeps expanding in the positive potential direction with the increase of Li^+ concentration, reaching the maximum (−0.6 to +0.5 V) when the Li^+ concentration reaches above 5 M. Additionally, the redox peak shifts toward higher potentials with the increase of LiCl concentration. For example, the anodic redox peaks in 3 M H_2SO_4 and 10 M LiCl and in 3 M H_2SO_4 and sat-LiCl remained around 0 V, which was nearly 0.35 V higher than the redox peak in H_2SO_4. Interestingly, another peak located at 0.32 V appeared when the electrolytes were saturated, possibly due to the intercalation of solvated Li^+ (Figure 3b).

Remarkably, unlike H_2SO_4, where the majority of the charge is stored within a negative potential region relative to the OCP, more charge contribution can be obtained from the potential region, which is more positive than the OCP in AWIS. Such an improvement is advantageous for achieving a broad voltage window while upholding high capacitance in a symmetric cell. Among all the electrolyte systems mentioned above, the largest potential window with the highest capacitance and charge contribution from the positive potential region is demonstrated in 3 M H_2SO_4 and 10 M LiCl AWIS. Therefore, the AWIS electrolytes based on 10 M LiCl were further studied.

Figure 3c illustrates the CV curves of $Ti_3C_2T_x$ in H_2SO_4 and 10 M LiCl AWIS. The capacitance also shows an increasing trend with more H^+ present in the electrolytes. Specifically, a

https://doi.org/10.1021/acsami.4c08094
ACS Appl. Mater. Interfaces 2024, 16, 55189−55197

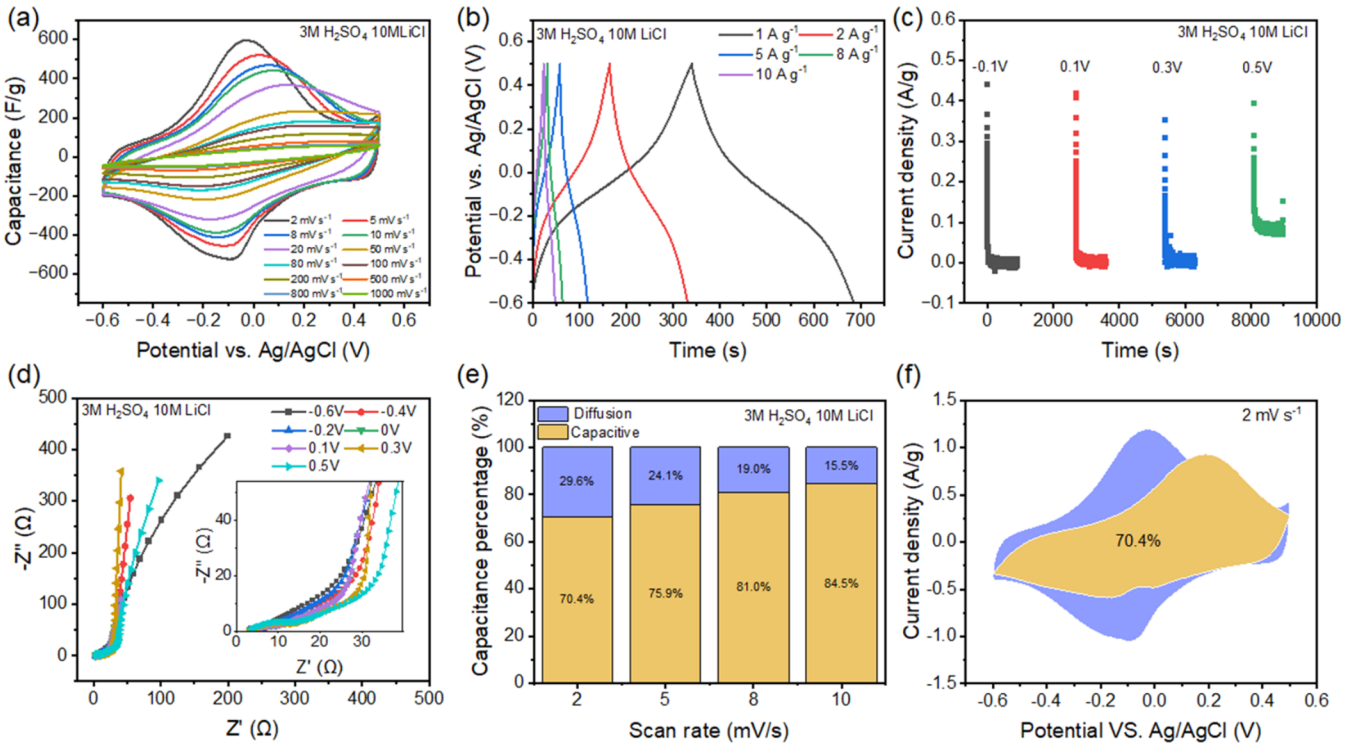

Figure 5. (a) Cyclic voltammograms of $Ti_3C_2T_x$ collected in 3 M H_2SO_4 and 10 M LiCl electrolyte at sweep speeds ranging from 2 to 1000 mV s^{-1} and (b) galvanostatic charge−discharge curves at different current densities; (c) chronoamperometry data and (d) Nyquist plots collected at different potentials in 3 M H_2SO_4 and 10 M LiCl. (e, f) Comparison of the contribution of a nondiffusion controlled process (capacitance) to the total current of $Ti_3C_2T_x$ at a scan rate of 2−10 mV s^{-1}.

high capacitance of 276.84 F g^{-1} can be obtained in 3 M H_2SO_4 and 10 M LiCl AWIS. Interestingly, a small overpotential is observed regardless of the H^+ concentration, even with a low H^+ concentration of 0.2 M (0.1 M H_2SO_4), unlike the H_2SO_4 and sat-LiCl AWIS electrolyte.

To better understand this behavior, Nyquist plots in 10 M LiCl AWIS with different H_2SO_4 concentrations were collected (Figure 3d). By slightly increasing the H_2SO_4 concentration, the internal resistance of the electrolyte increases compared to that of 10 M LiCl, indicating that a small amount of H^+ affects the diffusion of Li^+. In contrast, the addition of a large amount of H_2SO_4 decreases the internal resistance of the solution. When the concentration of H_2SO_4 exceeds 0.5 M, the internal resistance of the electrolyte decreases with increased H^+ content.

To investigate the charge storage mechanism of $Ti_3C_2T_x$ in the AWIS electrolyte, in situ XRD analysis was carried out to monitor changes in the interlayer spacing of the $Ti_3C_2T_x$ electrode during electrochemical cycling in 3 M H_2SO_4 and AWIS electrolytes at a scan rate of 0.2 mV s^{-1}. A total of three CV cycles were performed. The second CV cycle result, which was relatively stable, was selected for in situ XRD analysis (Figure S4). In 3 M H_2SO_4 electrolyte, a nonlinear change of MXene *d*-spacing with an overall change of 0.46 Å in the *d*-spacing upon cycling was observed, which is in general agreement with the previous report in 1 M H_2SO_4.[38] The *d*-spacing of $Ti_3C_2T_x$ is 14.06 Å at 0.1 V vs Ag, which decreases to 13.88 Å when the potential decreases to −0.45 V, due to the Coulombic attraction between intercalated H^+ with the negatively charged MXene surface. From −0.45 to −0.7 V, the *d*-spacing is gradually increased to 14.41 Å, which is possibly attributed to the steric effect when more hydrated H^+ is inserted in the *d*-spacing. A further expansion of *d*-spacing to 14.52 Å is observed over a further cathodic scan to −0.8 V (Figure S5). In contrast, an abrupt expansion of 1.9 Å in *d*-spacing, corresponding to the intercalation of solvated Li^+ ions, was observed at the onset reduction peak potential in LiCl WIS electrolyte.[30]

Figure 4 shows the *in situ* XRD pattern of $Ti_3C_2T_x$ in 3 M H_2SO_4 and 10 M LiCl AWIS electrolyte. During discharging, the *d*-spacing expanded slightly from 13.67 to 13.69 Å when the potential decreased from 0.6 to 0.47 V and remained unchanged until 0.29 V. A continuous shrinkage of the *d*-spacing to 13.46 Å was observed from 0.29 to 0.03 V where the cathodic peak was located. The *d*-spacing remained unchanged upon further cycling to −0.4 V. A reversible expansion behavior in the *d*-spacing was observed at the anodic peak potential during the charging process. A continuous shrinkage of 0.21 Å at the reduction peak potential during the cathodic scan in AWIS differs from the observation in both 3 M H_2SO_4 and WIS electrolytes, where the H^+ and solvated Li^+ intercalation dominate, respectively, indicating a distinct intercalation behavior of $Ti_3C_2T_x$ in AWIS electrolyte. The small *d*-spacing change is favorable for maintaining the MXene electrode's structural integrity, which may be beneficial for cycling stability. More advanced characterizations, for instance, electrochemical quartz crystal microbalances, are needed to identify the intercalated species.

The CV curves of $Ti_3C_2T_x$ in 3 M H_2SO_4 and 10 M LiCl at different scan rates are shown in Figure 5a, demonstrating excellent electrochemical performance with a capacity of 276.84 F g^{-1} at a sweep rate of 2 mV s^{-1}. The capacitance retention is 35.75% at a sweep rate of 100 mV s^{-1} (Figure S6). Galvanostatic charge−discharge (GCD) curves (Figure 5b)

https://doi.org/10.1021/acsami.4c08094
ACS Appl. Mater. Interfaces 2024, 16, 55189−55197

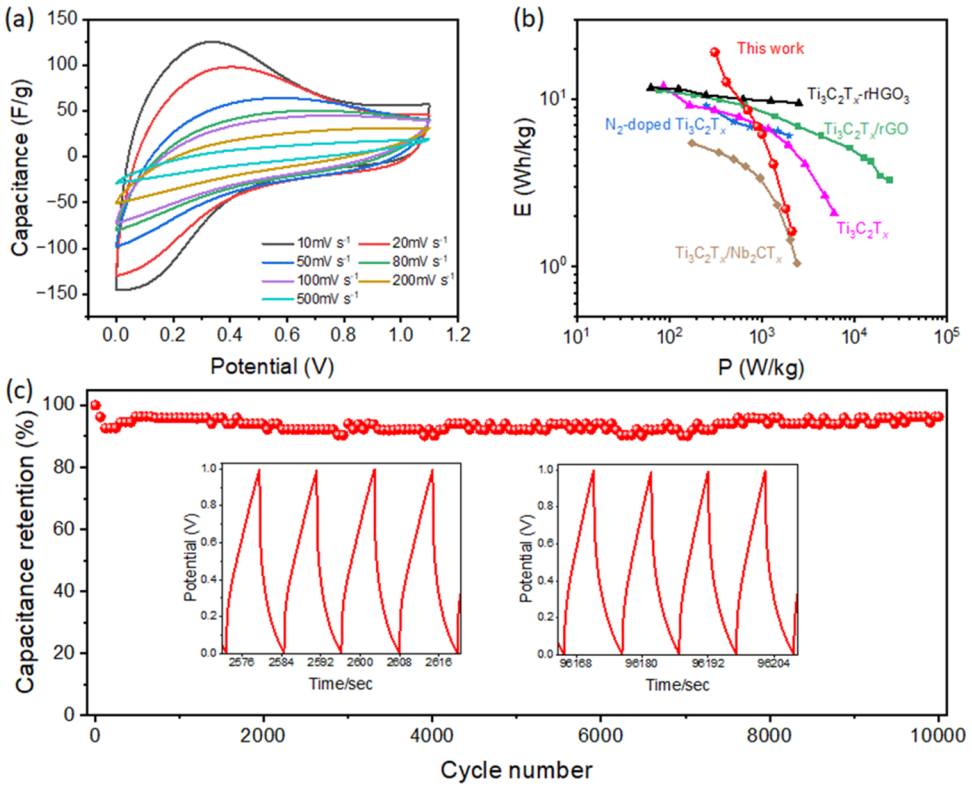

Figure 6. (a) Cyclic voltammograms of $Ti_3C_2T_x$-based symmetric supercapacitor with a 1:1 mass ratio of positive and negative electrodes in AWIS (3 M H_2SO_4 and 10 M LiCl) at 10−1000 mV s^{-1}; (b) Ragone plot of the symmetric supercapacitor in this work versus other MXene-based symmetric supercapacitors compared in the literature; (c) $Ti_3C_2T_x$-based capacitance retention of the symmetric supercapacitor at a current density of 4 A g^{-1} after 10,000 cycles in AWIS.

also exhibit a longer charge/discharge duration concerning 19.8 M LiCl and a small voltage drop in the discharging curve, suggesting a smaller internal resistance of $Ti_3C_2T_x$ in 3 M H_2SO_4 and 10 M LiCl.[39] Chronoamperometry results at different potentials show that the steady-state current densities are minuscule at all potentials except below 0.5 V. When the potential arrives at 0.5 V, a small but steady current density is detected, implying the splitting, where a small amount of oxidation occurs, suggesting that the contribution from other side reactions is negligible (Figure 5c). In addition, the Nyquist plots at different potentials (Figure 5d) show that the low-frequency regions of the potentials are close to vertical slopes, which is close to the ideal capacitive electrochemical process except for a slight deviation at the −0.6 V potential.

By comparing the $Ti_3C_2T_x$ electrodes at scan rates of 2−10 mV s^{-1} (Figure 5e,f), the contributions of diffusion-controlled and nondiffusion processes to the total current in the CV curves were studied (Figure S8). It can be seen that the diffusion control process has a significant effect on the total current. As the scanning speed increases, the contribution of the diffusion control process to the capacitance decreases. This is mainly because the charge transfer during the diffusion process is slow and it cannot respond quickly to potential changes at high scanning speeds. Therefore, the capacitance contributed by this current will sharply decay with an increasing scanning speed.

To demonstrate the advantage of an AWIS MXene-based symmetric supercapacitor, a two-electrode cell was assembled with $Ti_3C_2T_x$ in 3 M H_2SO_4 and 10 M LiCl electrolyte. The positive and negative mass ratios (p/n ratios) were optimized to achieve the best performance (Figure S7). Surprisingly, the optimal mass ratio is 1:1, which means a symmetric supercapacitor design will be a good choice for AWIS electrolytes. As a result, a lot of practical advantages for symmetric devices can be reserved such as facile assembly and nonpolarity. Figure 6a shows the CV curves of the symmetric supercapacitor of $Ti_3C_2T_x$ with a p/n ratio of 1:1 at different sweep speeds. A pair of redox peaks can be observed, which is consistent with the results of the three-electrode tests shown in Figure 5a. The symmetric cell showed a high capacitance of 112.3 F g^{-1} and can be operated in a wide voltage window of 1.1 V in the AWIS electrolyte, resulting in significant enhancement in the energy density of supercapacitors. Figure 6b shows the Ragone plots of energy density and power density of this work in comparison with those of other symmetric supercapacitors. The maximum energy density of the $Ti_3C_2T_x$-based symmetric supercapacitor in AWIS reaches 19.1 Wh kg^{-1}, which is almost twice that of other symmetric supercapacitors when the power density is 312.5 W kg^{-1}, and 1.36 Wh kg^{-1} when the power density reaches 2.13 kW kg^{-1}. The maximum energy density of $Ti_3C_2T_x$-based symmetric supercapacitors in AWIS is higher relative to other $Ti_3C_2T_x$-based supercapacitors, e.g., the maximum energy density of $Ti_3C_2T_x$ in 3 M H_2SO_4 is 11.97 Wh kg^{-1}, whereas the highest energy density of rGO-doped $Ti_3C_2T_x$ is 10.5 Wh kg^{-1};[40] the highest energy density of MXene-holy graphene ($Ti_3C_2T_x$-rHGO) is 11.7 Wh kg^{-1},[41] N-doped $Ti_3C_2T_x$ is 9.17 Wh kg^{-1},[42] and $Ti_3C_2T_x$ mixed with Nb_2CT_x is 5.47 Wh kg^{-1}.[43]

The cycling stability of the AWIS electrolyte was evaluated by repeating the charging and discharging of $Ti_3C_2T_x$-based symmetric supercapacitors in AWIS 10,000 times at a current density of 4 A g^{-1}. As can be seen in Figure 6c, the $Ti_3C_2T_x$-

https://doi.org/10.1021/acsami.4c08094
ACS Appl. Mater. Interfaces 2024, 16, 55189−55197

based symmetric supercapacitor has excellent cycling stability with a capacitance retention of 96.3% after 10,000 cycles. It is worth noting that the cycling stability of $Ti_3C_2T_x$ in AWIS electrolyte is significantly higher than that in 10 M LiCl (24.90% retention) and 3 M H_2SO_4 electrolytes (81.24% retention) (Figure S9), implying that AWIS electrolytes are much better choices for wide voltage supercapacitors with MXenes as electrodes. The enhanced cycling stability in the AWIS electrolyte is possibly attributed to the small *d*-spacing change upon cycling.

CONCLUSIONS

In summary, the electrolyte combining H^+ and Li^+ can substantially improve the performance of $Ti_3C_2T_x$-based symmetric supercapacitors, and the addition of Li^+ causes the potential window of $Ti_3C_2T_x$ to expand in the positive potential direction. The potential window expands to a maximum value of 1.1 V after the Li^+ concentration reaches 5 M. With the increase of Li^+ concentration, the anodic redox peak gradually shifts to the positive potential direction, and the position of the anodic redox peak reaches about 0 V (vs Ag/AgCl) after Li^+ reaches saturation. The *in situ* XRD results show that $Ti_3C_2T_x$ has obvious layer spacing changes only at 0.4 to 0.5 V (vs Ag) in AWIS, and the *d*-spacing is almost unchanged at other potentials, which is a different charge storage mechanism from that in 3 M H_2SO_4 and 19.8 M LiCl. $Ti_3C_2T_x$-based symmetric supercapacitors exhibit superior electrochemical performance relative to other supercapacitors in the AWIS electrolyte and have excellent cycling stability.

The findings in this work shed light on improving the energy density of MXene-based supercapacitors effectively by simply formulating different electrolytes. Based on the results of this work, various mixed electrolytes can be further explored in the future for developing high performance MXene-supercapacitors beyond high-energy density. The synergistic effect of the electrolyte components can be systematically studied for better understanding the charge storage mechanism of MXenes in mixed electrolytes, based on which a higher and more comprehensive electrochemical performance can be achieved.

EXPERIMENTAL SECTION

Materials. One gram of Ti_3AlC_2 powder (from Jilin 11 Technology Co., Ltd.) was etched in a mixture of 6 mL of H_2O, 12 mL of 12 M HCl, and 2.5 mL of HF for 24 h at a stirring speed of 750 rpm and a temperature of 35 °C. The powder was then washed by the HF etching method. After etching, it was washed with deionized water until pH ∼ 6. After that, the washed $Ti_3C_2T_x$ was dispersed in 60 mL of aqueous solution containing 1 g of LiCl for intercalation at a temperature of 35 °C with a stirring speed of 750 rpm. Finally, it was washed with deionized water, and the supernatant containing well-dispersed monolayers of MXene was collected by centrifugation several times.

The well-dispersed monolayer $Ti_3C_2T_x$ dispersion was filtered through a 45 μm nylon-6 membrane, and after filtration, the membrane was placed in a vacuum drying oven overnight to obtain the final vacuum-filtered $Ti_3C_2T_x$ film.

Materials Characterization. X-ray diffraction (XRD) spectra of $Ti_3C_2T_x$ thin films as well as $Ti_3C_2T_x$ thin films after immersion in the electrolyte were collected on a Rigaku SmartLab (45 kV, 200 mA) diffractometer using Cu Kα radiation. The *in situ* X-ray diffraction cell had a $Ti_3C_2T_x$ film (D = 8 mm) as the working electrode, a graphite electrode (1 cm × 1 cm) as the counter electrode, and a silver wire as the reference electrode. *In situ* X-ray diffraction (XRD) was carried out using an X'Pert Pro diffractometer (PANalytical, 45 kV and 40 mA) and Cu Kα (λ = 1.54 Å) radiation. Cyclic voltammetry (CV) was carried out using a Lahne G340A potentiostat at an open-circuit potential of 0.2 mV s^{-1}, and XRD patterns of $Ti_3C_2T_x$ electrodes were collected in steps of 0.01° over the range 2θ = 4−15°. CV scans in 3 M H_2SO_4 were recorded in the range of −0.8−0.1 V, while those in 3 M H_2SO_4 10 M LiCl were recorded in the range of −0.4−0.6 V (reference electrode: Ag wire).

Electrochemical Testing. Vacuum-filtered $Ti_3C_2T_x$ films were cut into 5 mm diameter discs to be used as electrode materials. The activated carbon electrode used in this work was obtained by mixing activated carbon (YP-50) powder with PTFE in a ratio of 95:5 by mass. First, a certain mass of activated carbon was dispersed in deionized water, and after that PTFE emulsion was added slowly in proportion to the mixing, following which vacuum filtration was carried out to obtain a film with a thickness of 100−150 μm by roller pressing, and then it was left to dry naturally to obtain the activated carbon electrode.

In the Swagelok battery, a $Ti_3C_2T_x$ film was used as the working electrode, the activated carbon electrode as the counter electrode, Ag/AgCl (saturated KCl) as the reference electrode, and the glassy carbon electrode as the current collector. In the three-electrode system, the working electrode was separated from the counter electrode by a Celgard film. For the two-cell system, the $Ti_3C_2T_x$ film was used as the positive and negative electrodes, and the cell was sealed with a Parafilm sealing film. Both two-electrode and three-electrode cells were rested for 12 h before electrochemical testing.

The electrochemical performance was tested on a CHI760e electrochemical workstation. Chronoamperometry tests were carried out by applying a constant voltage (−0.1, 0.1, 0.2, 0.3, 0.4, and 0.5 V (vs Ag/AgCl)) to the three-electrode cell and recording the response of current density over time. Cyclic voltammetry (CV) tests were performed at scan rates of 2−1000 mV s^{-1}; constant current charge/discharge (GCD) tests were performed at current densities ranging from 1 to 10 A g^{-1}, and the AC impedance (EIS) was obtained by testing at frequencies from 0.1 Hz to 10 kHz.

The gravimetric capacitance (C_g) was calculated from the CV scan curve based on the following expression

$$C_g\ (\mathrm{F\ g^{-1}}) = \frac{\int i\mathrm{d}V}{v \cdot m \cdot V} \tag{1}$$

where i is the current (A) that changes at time t, V is the potential window (V) of the CV scan, v stands for the scan rate (mV s^{-1}), and m is the mass of the active material (g) on the working electrode for the three-electrode cell and is the mass of the active material on both electrodes for a two-electrode cell.

The energy density (E) of the full cell was estimated based on the following expression

$$E\ (\mathrm{Wh\ kg^{-1}}) = \frac{1}{2}CV^2 \tag{2}$$

where C is the gravimetric capacitance (F g^{-1}) and V is the voltage window (V) of the CV scan.[44,45]

The power density (P) of the full cell was estimated based on the following expression

$$P = \frac{E}{\Delta t} \tag{3}$$

where E is the energy density (W kg^{-1}) and Δt is the charge/discharge time (s).[46,47]

ASSOCIATED CONTENT

Supporting Information

The Supporting Information is available free of charge at https://pubs.acs.org/doi/10.1021/acsami.4c08094.

SEM images of $Ti_3C_2T_x$; GCD, CA, and Nyquist curves of $Ti_3C_2T_x$ thin-film electrodes in AWIS electrolyte; *in situ* XRD curves in H_2SO_4; and CV curves of $Ti_3C_2T_x$−$Ti_3C_2T_x$ devices with different mass ratios (PDF)

https://doi.org/10.1021/acsami.4c08094
ACS Appl. Mater. Interfaces 2024, 16, 55189−55197

AUTHOR INFORMATION

Corresponding Authors

Jiaji Cheng − *School of Materials Science Engineering, Hubei University, Wuhan, Hubei 430062, China*; Email: jiajicheng@huhu.edu.cn

Baomin Xu − *Department of Materials Science and Engineering, Southern University of Science and Technology, Shenzhen, Guangdong 518055, China*; Email: xubm@sustech.edu.cn

Xuehang Wang − *Department of Radiation Science and Technology, Delft University of Technology, Delft 2629 JB, The Netherlands*; Email: x.wang-22@tudelft.nl

Jun Tang − *College of New Materials and New Energy, Shenzhen Technology University, Shenzhen, Guangdong 518118, China*; orcid.org/0000-0001-6229-2051; Email: tangjun3@sztu.edu.cn

Authors

Chengzhi Yuan − *College of New Materials and New Energy, Shenzhen Technology University, Shenzhen, Guangdong 518118, China; School of Materials Science Engineering, Hubei University, Wuhan, Hubei 430062, China*

Chaofan Chen − *Department of Radiation Science and Technology, Delft University of Technology, Delft 2629 JB, The Netherlands*

Zhiwei Yang − *College of New Materials and New Energy, Shenzhen Technology University, Shenzhen, Guangdong 518118, China*

Ji Weng − *College of New Materials and New Energy, Shenzhen Technology University, Shenzhen, Guangdong 518118, China*

Shuhui Tan − *College of New Materials and New Energy, Shenzhen Technology University, Shenzhen, Guangdong 518118, China*

Renzhong Hou − *College of New Materials and New Energy, Shenzhen Technology University, Shenzhen, Guangdong 518118, China*

Tao Cao − *College of New Materials and New Energy, Shenzhen Technology University, Shenzhen, Guangdong 518118, China*

Zeguo Tang − *College of New Materials and New Energy, Shenzhen Technology University, Shenzhen, Guangdong 518118, China*; orcid.org/0000-0001-8823-8651

Wei Chen − *College of Engineering Physics, Shenzhen Technology University, Shenzhen, Guangdong 518118, China*; orcid.org/0000-0001-9550-0523

Complete contact information is available at: https://pubs.acs.org/10.1021/acsami.4c08094

Author Contributions

#C.Y., C.C., and Z.Y. contributed equally to this work.

Notes

The authors declare no competing financial interest.

ACKNOWLEDGMENTS

This research was financially supported by the National Natural Science Foundation of China (NSFC) (No. 52302294), Key Fundamental Research Project funding from the Shenzhen Science and Technology Innovation Committee/Shenzhen Science and Technology Program (No. JCYJ20220818100406014), GuangDong Basic and Applied Basic Research Foundation (No. 2022A1515111140), and Natural Science Foundation of Top Talent of SZTU (No. GDRC202348).

REFERENCES

(1) Lukatskaya, M. R.; Kota, S.; Lin, Z. F.; Zhao, M. Q.; Shpigel, N.; Levi, M. D.; Halim, J.; Taberna, P. L.; Barsoum, M.; Simon, P.; Gogotsi, Y. Ultra-high-rate pseudocapacitive energy storage in two-dimensional transition metal carbides. *Nat. Energy* **2017**, *2* (8), No. 17105.

(2) Spurling, D.; Krüger, H.; Kohlmann, N.; Rasch, F.; Kremer, M. P.; Kienle, L.; Adelung, R.; Nicolosi, V.; Schütt, F. 3D networked MXene thin films for high performance supercapacitors. *Energy Storage Mater.* **2024**, *65*, No. 103148.

(3) Wang, K. L.; Zheng, B. C.; Mackinder, M.; Baule, N.; Qiao, H.; Jin, H.; Schuelke, T.; Fan, Q. H. Graphene wrapped MXene via plasma exfoliation for all-solid-state flexible supercapacitors. *Energy Storage Mater.* **2019**, *20*, 299−306.

(4) Feng, S.; Wang, X.; Wang, M.; Bai, C.; Cao, S.; Kong, D. Crumpled MXene Electrodes for Ultrastretchable and High-Area-Capacitance Supercapacitors. *Nano Lett.* **2021**, *21* (18), 7561−7568.

(5) Liang, Q.; Liu, K.; Xu, T.; Wang, Y.; Zhang, M.; Zhao, Q.; Zhong, W.; Cai, X. M.; Zhao, Z.; Si, C. Interfacial Modulation of $Ti_3C_2T_x$ MXene by Cellulose Nanofibrils to Construct Hybrid Fibers with High Volumetric Specific Capacitance. *Small* **2023**, *20*, No. 2307344.

(6) Li, S.; Chang, T.-H.; Li, Y.; Ding, M.; Yang, J.; Chen, P.-Y. Stretchable $Ti_3C_2T_x$ MXene microsupercapacitors with high areal capacitance and quasi-solid-state multivalent neutral electrolyte. *J. Mater. Chem. A* **2021**, *9* (8), 4664−4672.

(7) Tan, J.; Fan, B.; Zhang, P.; Wei, Y.; Soomro, R. A.; Zhao, X.; Kumar, J.; Qiao, N.; Xu, B. Ultralong Stability of Ti3C2Tx-MXene Dispersion Through Synergistic Regulation of Storage Environment and Defect Capping with Tris-HCl Buffering. *Small Methods* **2024**, No. 2301689.

(8) Luo, J.; Matios, E.; Wang, H.; Tao, X.; Li, W. Interfacial structure design of MXene-based nanomaterials for electrochemical energy storage and conversion. *InfoMat* **2020**, *2* (6), 1057−1076.

(9) Liu, H.; Xu, Z.; Cao, B.; Xin, Z.; Lai, H.; Gao, S.; Xu, B.; Yang, J. L.; Xiao, T.; Zhang, B.; Fan, H. J. Marangoni-Driven Self-Assembly MXene As Functional Membrane Enables Dendrite-Free and Flexible Zinc-Iodine Pouch Cells. *Adv. Energy Mater.* **2024**, *14* (26), No. 2400318.

(10) Luo, J.; Lu, X.; Matios, E.; Wang, C.; Wang, H.; Zhang, Y.; Hu, X.; Li, W. Tunable MXene-Derived 1D/2D Hybrid Nanoarchitectures as a Stable Matrix for Dendrite-Free and Ultrahigh Capacity Sodium Metal Anode. *Nano Lett.* **2020**, *20* (10), 7700−7708.

(11) Luo, J.; Wang, C.; Wang, H.; Hu, X.; Matios, E.; Lu, X.; Zhang, W.; Tao, X.; Li, W. Pillared MXene with Ultralarge Interlayer Spacing as a Stable Matrix for High Performance Sodium Metal Anodes. *Adv. Funct. Mater.* **2018**, *29* (3), No. 1805946.

(12) Luo, J.; Zheng, J.; Nai, J.; Jin, C.; Yuan, H.; Sheng, O.; Liu, Y.; Fang, R.; Zhang, W.; Huang, H.; et al. Atomic Sulfur Covalently Engineered Interlayers of Ti_3C_2 MXene for Ultra-Fast Sodium-Ion Storage by Enhanced Pseudocapacitance. *Adv. Funct. Mater.* **2019**, *29* (10), No. 1808107.

(13) Zhou, S.; Zhang, P.; Li, Y.; Feng, L.; Xu, M.; Soomro, R. A.; Xu, B. Ultrastable Organic Anode Enabled by Electrochemically Active MXene Binder toward Advanced Potassium Ion Storage. *ACS Nano* **2024**, *18* (24), 16027−16040.

(14) Gao, Q.; Sun, W.; Ilani-Kashkouli, P.; Tselev, A.; Kent, P. R. C.; Kabengi, N.; Naguib, M.; Alhabeb, M.; Tsai, W.-Y.; Baddorf, A. P.; et al. Tracking ion intercalation into layered Ti_3C_2 MXene films across length scales. *Energy Environ. Sci.* **2020**, *13* (8), 2549−2558.

(15) Lukatskaya, M. R.; Mashtalir, O.; Ren, C. E.; Dall'Agnese, Y.; Rozier, P.; Taberna, P. L.; Naguib, M.; Simon, P.; Barsoum, M. W.; Gogotsi, Y. Cation intercalation and high volumetric capacitance of two-dimensional titanium carbide. *Science* **2013**, *341* (6153), 1502−1505.

(16) Peng, Y. Y.; Akuzum, B.; Kurra, N.; Zhao, M. Q.; Alhabe, M.; Anasori, B.; Kumbur, E. C.; Alshareef, H. N.; Ger, M. D.; Gogotsi, Y. All-MXene (2D titanium carbide) solid-state microsupercapacitors for on-chip energy storage. *Energy Environ. Sci.* **2016**, *9* (9), 2847−2854.
(17) Wang, F.; Xiao, S.; Hou, Y.; Hu, C.; Liu, L.; Wu, Y. Electrode materials for aqueous asymmetric supercapacitors. *RSC Adv.* **2013**, *3* (32), 13059−13084.
(18) Zhao, R.; Wang, M.; Zhao, D.; Li, H.; Wang, C.; Yin, L. Molecular-Level Heterostructures Assembled from Titanium Carbide MXene and Ni−Co−Al Layered Double-Hydroxide Nanosheets for All-Solid-State Flexible Asymmetric High-Energy Supercapacitors. *ACS Energy Lett.* **2018**, *3* (1), 132−140.
(19) Ghazaly, A. E.; Zheng, W.; Halim, J.; Tseng, E. N.; Persson, P. O.; Ahmed, B.; Rosen, J. Enhanced supercapacitive performance of $Mo_{1.33}C$ MXene based asymmetric supercapacitors in lithium chloride electrolyte. *Energy Storage Mater.* **2021**, *41*, 203−208.
(20) Ma, L.; Zhao, T. C.; Xu, F.; You, T. T.; Zhang, X. M. A dual utilization strategy of lignosulfonate for MXene asymmetric supercapacitor with high area energy density. *Chem. Eng. J.* **2021**, *405*, No. 126649.
(21) Jiang, Q.; Kurra, N.; Alhabeb, M.; Gogotsi, Y.; Alshareef, H. N. All Pseudocapacitive Mxene-RuO_2 Asymmetric Supercapacitors. *Adv. Energy Mater.* **2018**, *8* (13), No. 1703043.
(22) Wei, Y.; Zheng, M.; Luo, W.; Dai, B.; Ren, J.; Ma, M.; Li, T.; Ma, Y. All pseudocapacitive MXene-MnO_2 flexible asymmetric supercapacitor. *J. Energy Storage* **2022**, *45*, No. 103715.
(23) Couly, C.; Alhabeb, M.; Van Aken, K. L.; Kurra, N.; Gomes, L.; Navarro-Suárez, A. M.; Anasori, B.; Alshareef, H. N.; Gogotsi, Y. Asymmetric Flexible MXene-Reduced Graphene Oxide Micro-Supercapacitor. *Adv. Electron. Mater.* **2018**, *4* (1), No. 1700339.
(24) Conway, B. E. *Electrochemical Supercapacitors: Scientific Fundamentals and Technological Applications*; Springer: New York, NY, 1999.
(25) Wang, G. N.; Guo, S. Y.; Wu, Y.; Wu, J. Q.; Zhang, F.; Li, L.; Zhang, M. Y.; Yao, C. B.; Gómez-García, C. J.; Wang, T. Y.; et al. POMCPs with Novel Two Water-Assisted Proton Channels Accommodated by MXenes for Asymmetric Supercapacitors. *Small* **2022**, *18* (29), No. 2202087.
(26) Liu, S.; Zeng, T.; Zhang, Y.; Wan, Q.; Yang, N. Coupling $W_{18}O_{49}$/$Ti_3C_2T_x$ MXene Pseudocapacitive Electrodes with Redox Electrolytes to Construct High-Performance Asymmetric Supercapacitors. *Small* **2022**, *18* (52), No. 2204829.
(27) Pan, Z.; Cao, F.; Hu, X.; Ji, X. A facile method for synthesizing CuS decorated Ti_3C_2 MXene with enhanced performance for asymmetric supercapacitors. *J. Mater. Chem. A* **2019**, *7* (15), 8984−8992.
(28) Zhu, K.; Jin, Y.; Du, F.; Gao, S.; Gao, Z.; Meng, X.; Chen, G.; Wei, Y.; Gao, Y. Synthesis of Ti_2CT_x MXene as electrode materials for symmetric supercapacitor with capable volumetric capacitance. *J. Energy Chem.* **2019**, *31*, 11−18.
(29) Xu, H. J.; Fan, J. X.; Su, H.; Liu, C. F.; Chen, G.; Dall'Agnese, Y.; Gao, Y. Metal Ion-Induced Porous MXene for All-Solid-State Flexible Supercapacitors. *Nano Lett.* **2023**, *23* (1), 283−290.
(30) Wang, X.; Mathis, T. S.; Sun, Y.; Tsai, W. Y.; Shpigel, N.; Shao, H.; Zhang, D.; Hantanasirisakul, K.; Malchik, F.; Balke, N.; et al. Titanium Carbide MXene Shows an Electrochemical Anomaly in Water-in-Salt Electrolytes. *ACS Nano* **2021**, *15* (9), 15274−15284.
(31) Wang, X.; Mathis, T. S.; Li, K.; Lin, Z.; Vlcek, L.; Torita, T.; Osti, N. C.; Hatter, C.; Urbankowski, P.; Sarycheva, A.; et al. Influences from solvents on charge storage in titanium carbide MXenes. *Nat. Energy* **2019**, *4* (3), 241−248.
(32) Hu, M.; Li, Z.; Hu, T.; Zhu, S.; Zhang, C.; Wang, X. High-Capacitance Mechanism for $Ti_3C_2T_x$ MXene by in Situ Electrochemical Raman Spectroscopy Investigation. *ACS Nano* **2016**, *10* (12), 11344−11350.
(33) Johnson, D.; Hansen, K.; Yoo, R.; Djire, A. Elucidating the Charge Storage Mechanism on $Ti_3C_2T_x$ MXene through In Situ Raman Spectroelectrochemistry. *ChemElectroChem* **2022**, *9* (18), No. e202200555.
(34) Zhang, D.; Wang, R.; Wang, X.; Gogotsi, Y. In situ monitoring redox processes in energy storage using UV−Vis spectroscopy. *Nat. Energy* **2023**, *8* (6), 567−576.
(35) Ling, Z.; Ren, C. E.; Zhao, M. Q.; Yang, J.; Giammarco, J. M.; Qiu, J.; Barsoum, M. W.; Gogotsi, Y. Flexible and conductive MXene films and nanocomposites with high capacitance. *Proc. Natl. Acad. Sci. U.S.A.* **2014**, *111* (47), 16676−16681.
(36) Wang, B.; Xie, Y.; Liu, T.; Luo, H.; Wang, B.; Wang, C.; Wang, L.; Wang, D.; Dou, S.; Zhou, Y. $LiFePO_4$ quantum-dots composite synthesized by a general microreactor strategy for ultra-high-rate lithium ion batteries. *Nano Energy* **2017**, *42*, 363−372.
(37) Mathis, T. S.; Kurra, N.; Wang, X. H.; Pinto, D.; Simon, P.; Gogotsi, Y. Energy Storage Data Reporting in Perspective-Guidelines for Interpreting the Performance of Electrochemical Energy Storage Systems. *Adv. Energy Mater.* **2019**, *9* (39), No. 1902007.
(38) Mu, X. P.; Wang, D. S.; Du, F.; Chen, G.; Wang, C. Z.; Wei, Y. J.; Gogotsi, Y.; Gao, Y.; Dall'Agnese, Y. Revealing the Pseudo-Intercalation Charge Storage Mechanism of MXenes in Acidic Electrolyte. *Adv. Funct. Mater.* **2019**, *29* (29), No. 1902953.
(39) Vicentini, R.; Da Silva, L. M.; Cecilio, E. P., Junior; Alves, T. A.; Nunes, W. G.; Zanin, H. How to Measure and Calculate Equivalent Series Resistance of Electric Double-Layer Capacitors. *Molecules* **2019**, *24* (8), No. 1452.
(40) Yan, J.; Ren, C. E.; Maleski, K.; Hatter, C. B.; Anasori, B.; Urbankowski, P.; Sarycheva, A.; Gogotsi, Y. Flexible MXene/Graphene Films for Ultrafast Supercapacitors with Outstanding Volumetric Capacitance. *Adv. Funct. Mater.* **2017**, *27* (30), No. 1701264.
(41) Fan, Z.; Wang, Y.; Xie, Z.; Wang, D.; Yuan, Y.; Kang, H.; Su, B.; Cheng, Z.; Liu, Y. Modified MXene/Holey Graphene Films for Advanced Supercapacitor Electrodes with Superior Energy Storage. *Adv. Sci.* **2018**, *5* (10), No. 1800750.
(42) Cai, M.; Wei, X.; Huang, H.; Yuan, F.; Li, C.; Xu, S.; Liang, X.; Zhou, W.; Guo, J. Nitrogen-doped $Ti_3C_2T_x$ MXene prepared by thermal decomposition of ammonium salts and its application in flexible quasi-solid-state supercapacitor. *Chem. Eng. J.* **2023**, *458*, No. 141338.
(43) Li, Z. M.; Dall'Agnese, Y.; Guo, J.; Huang, H. F.; Liang, X. Q.; Xu, S. K. Flexible freestanding all-MXene hybrid films with enhanced capacitive performance for powering a flex sensor. *J. Mater. Chem. A* **2020**, *8* (32), 16649−16660.
(44) Fan, W.; Wang, Q.; Rong, K.; Shi, Y.; Peng, W.; Li, H.; Guo, Z.; Xu, B. B.; Hou, H.; Algadi, H.; et al. MXene Enhanced 3D Needled Waste Denim Felt for High-Performance Flexible Supercapacitors. *Nano-Micro Lett.* **2023**, *16* (1), No. 36.
(45) Lu, C.; Li, A.; Zhai, T.; Niu, C.; Duan, H.; Guo, L.; Zhou, W. Interface design based on Ti3C2MXene atomic layers of advanced battery-type material for supercapacitors. *Energy Storage Mater.* **2020**, *26*, 472−482.
(46) Jin, W.-H.; Cao, G.-T.; Sun, J.-Y. Hybrid supercapacitor based on MnO2 and columned FeOOH using Li2SO4 electrolyte solution. *J. Power Sources* **2008**, *175* (1), 686−691.
(47) Lee, J. H.; Kim, H. K.; Baek, E.; Pecht, M.; Lee, S. H.; Lee, Y. H. Improved performance of cylindrical hybrid supercapacitor using activated carbon/niobium doped hydrogen titanate. *J. Power Sources* **2016**, *301*, 348−354.

https://doi.org/10.1021/acsami.4c08094
ACS Appl. Mater. Interfaces 2024, 16, 55189−55197